



ISSN: 0067-2904

Characterization of Calcinated Ni–Cu Ferrite Nanoparticles Synthesized by Citrate-gel Auto combustion Technique

Ibrahim F. Waheed¹, Thuraya Yarb Sabri², Najat A. Dahham^{*2}, Faten Haithum Mulud²

¹Department of Chemistry, College of Science, University of Tikrit, Tikrit, Iraq

²Department of Physics, College of Science, University of Tikrit, Tikrit, Iraq

Received: 7/3/2020

Accepted: 19/5/2020

Abstract

Citrate-gel auto combustion technique was used to synthesize nickel-copper mixed ferrite nanoparticles $Ni_xCu_{1-x}Fe_2O_4$ ($x= 0.0, 0.4, 1.0$) with different calcinating temperatures (200, 450, 650 and 850 °C). Structural, morphological, magnetic, and electrical properties were studied using X-ray diffraction (XRD), transmission electron microscopy (TEM), field emission scanning electron microscopy (FE-SEM), Fourier transform infrared spectroscopy (FTIR), vibrating sample magnetometer (VSM), and LCR meter in order to determine significant influences of Cu^{2+} cations content in nickel ferrite. The XRD patterns showed that all compositions had cubic spinels, except $CuFe_2O_4$ samples. The system structure in Cu-ferrite was deformed at 650 °C from a cubic to a tetragonal system with a secondary phase CuO. Lattice constant was decreased with increasing Cu^{2+} cations substitution in Ni-ferrites, while crystalline volume was increased. With the help of Debye-Scherrer's equation using XRD data, we found that the crystallite size at 850 °C is lying in the range from 38.70 to 48.00 nm. The FTIR spectrum of samples under investigation showed two significant absorption bands, which refer to the formation of a single-phase cubic spinel. The magnetization test revealed a soft ferromagnetic behavior for all the compositions sintered at 850 °C. The saturation magnetization (M_s) was decreased with the substitution by Cu^{2+} cations, while remnant magnetization (M_r) and coercivity (H_c) were increased in Cu-ferrite. The highest M_s value was 42.25 $emu.g^{-1}$ for Ni-ferrite, while the highest H_c value was 517.16 O_e for Cu-ferrite. The electrical measurement of samples showed an increase in the real dielectric constant and AC conductivity at a frequency range of 20Hz-3MHz with the addition of copper cations.

Keywords: Nickel-copper ferrite, Magnetic properties, dielectric properties

تشخيص الجسيمات النانوية لفرايت Cu–Ni المحضرة بتقنية الاحتراق التلقائي لجل السترات

ابراهيم فهد وحيد¹، ثريا يعرب صبري²، نجاة احمد دحام^{*2}، فaten هيثم مولود²

¹قسم الكيمياء، كلية العلوم، جامعة تكريت، تكريت، العراق.

²قسم الفيزياء، كلية العلوم، جامعة تكريت، تكريت، العراق

الخلاصة

تم استخدام تقنية الاحتراق التلقائي لسيترات-جل لتصنيع جسيمات الفرايت النانوية المختلطة من النيكل والنحاس ($x = 0.0, 0.4, 1.0$) $Ni_xCu_{1-x}Fe_2O_4$ بدرجات حرارة تليدين مختلفة (200, 450, 650, 850)°C. تمت دراسة الخواص التركيبية والمورفولوجية والمغناطيسية والكهربائية باستخدام

حيود الأشعة السينية (XRD) ، المجهر الإلكتروني النافذ (TEM) ، المجهر الإلكتروني الماسح ذو الانبعاث المجالي (FE-SEM) ، التحليل الطيفي بالأشعة تحت الحمراء (FTIR) ، مقياس المغناطيسية ذو العينة الاهتزازية (VSM) و مقياس LCR من أجل دراسة التأثير الكبير لتركيز الكاتيونات Cu^{2+} في الفريت النيكل. أظهرت أنماط حيود الأشعة السينية أن جميع التراكيب ذات مكعب مغزلي باستثناء عينات CuFe_2O_4 قد تشوه تركيب النظام في الفريت النحاس عند 650°C من المكعب إلى النظام رباعي القائم مع طور ثانوي CuO . يتناقص ثابت الشبكة مع زيادة استبدال كاتيونات Cu^{2+} في فريت النيكل ، بينما يزيد الحجم البلوري مع استبدال كاتيونات Cu^{2+} بمساعدة معادلة ديبي-شيرر وباستخدام بيانات حيود الأشعة السينية ، وجدنا أن حجم البلورة عند 850°C درجة مئوية يقع في المدى من 38.70 إلى 48.00 نانو متر. يُظهر طيف FTIR للعينة قيد البحث نطاقين مهمين من الامتصاص ، يشيران إلى تكوين المكعب المغزلي أحادي الطور. كشفت المغنطة عن السلوك الفيرو مغناطيسي اللين لجميع التراكيب الملدنة بدرجة 850°C . انخفضت مغناطيسية التشبع (Ms) مع استبدال كاتيونات Cu^{2+} ، بينما زادت المغناطيسية المتبقية (M_r) والمقاومة المغناطيسية القهرية (Hc) لفريت النحاس . أعلى قيمة Ms هي 42.25 emu.g^{-1} لفريت النيكل ، بينما أعلى قيمة لـ Hc هي 517.16 Oe لفريت النحاس. توضح القياسات الكهربائية للعينات الزيادة في ثابت العزل الكهربائي الحقيقي والتوصيلية المتناوبة بمدى تردد من 20 هيرتز إلى 3 ميغا هيرتز مع إضافة كاتيونات النحاس.

1. Introduction

In recent years, the ferrites family has gained a great importance among researchers, as these materials have been greatly desired in various electrical industries. They are electrically insulated and accompanied by high resistance, leading to their employment in changing magnetic fields because their loss of eddy currents is very slight. This feature made such materials more widely used in the applications of microwave and magnetic fluids [1], recording disks, transformer molds, gas sensors, and moisture sensors [2, 3]. The general formula for spinel ferrites is MFe_2O_4 , where M is a metallic divalent ion (e.g., Cu, Fe, Cd, Ni, Zn, etc.) [4]. Among the most famous ferrites are CuFe_2O_4 and NiFe_2O_4 , due to their inverse spinel structure. They have ferromagnetic behavior and wide device applications. The substitution of copper in nickel ferrite enhances the dielectric properties. Besides, it reduces the magnetic properties of nickel ferrite, which is useful in many device applications [5]. CuFe_2O_4 and NiFe_2O_4 were prepared by various methods, such as the ceramic method [6], electrodeposition method [7], hydrothermal reaction [8], oxidation precipitation [9], sol-gel method [10], and electrochemical method [11]. Among the best methods for preparing ferrite compounds is the self-combustion method for the gel, because it is easy to prepare, does not need high temperature, the interacting elements and the granular size of the powder nanoparticles can be controlled, and free from impurities [12]. The aim of the present work is to understand the role of Cu^{2+} cations in controlling the dielectric and magnetic behavior of Ni-ferrite. Therefore, a series of $\text{Ni}_x\text{Cu}_{1-x}\text{Fe}_2\text{O}_4$ ($x=0.0, 0.4, 1.0$) spinel ferrite samples were prepared and the consequent changes in several parameters, such as lattice constant, crystalline volume, density, saturation magnetization, dielectric permittivity, and dielectric loss tangent, were discussed in this paper. Furthermore, we investigated the effect of calcination temperature on the parameters above.

2. Experimental Part

2.1. Synthesis of $\text{Ni}_x\text{Cu}_{1-x}\text{Fe}_2\text{O}_4$ nanoparticles

The spinel samples of $\text{Ni}_x\text{Cu}_{1-x}\text{Fe}_2\text{O}_4$ were prepared with values of $x = 0.0, 0.4, 1.0$ using the citrate-gel auto combustion technique. Iron nitrate ($\text{Fe}(\text{NO}_3)_3 \cdot 9\text{H}_2\text{O}$), copper nitrate ($\text{Cu}(\text{NO}_3)_2 \cdot 3\text{H}_2\text{O}$), nickel nitrate ($\text{Ni}(\text{NO}_3)_2 \cdot 6\text{H}_2\text{O}$), Citric acid ($\text{C}_6\text{H}_8\text{O}_7 \cdot \text{H}_2\text{O}$), and ammonia (NH_3OH) were used as raw materials for preparing the compounds of $\text{Ni}_x\text{Cu}_{1-x}\text{Fe}_2\text{O}_4$ nanoparticles. A stoichiometric ratio of nickel nitrate (1.163 g) and ferric nitrate (3.232 g) was mixed in 50 ml deionized water. The molar ratio of nickel nitrate and ferric nitrate was 1:2. Citric acid was added as a fuel in the metal nitrate with a ratio of 3:1 under vigorous stirring conditions. The ferrite samples were successfully prepared by doping of Cu^{2+} with different molar ratios ($\text{Ni}_x\text{Cu}_{1-x}\text{Fe}_2\text{O}_4$, $x=0.0, 0.4, 1.0$) to nickel ferrite. Copper nitrate amounts that were added to nickel nitrate solution were 1.182 g and 0.177 g for molar ratios of 0.0 and 0.4, respectively. The pH value of the solution mixture was maintained at 8 by ammonia solution. The mixing process was continued to ensure complete mixing of

the solution and a good distribution of the components at room temperature. After that, the temperature was gradually raised and then fixed at 90°C with the stirring process continuing until the gel form was reached. After around 10 min the gel began to burn out to form a dry gel (Xerogel). The final burnt powders were then thermally calcinated at 200, 450, 650, and 850 °C for 3 h to obtain well-crystallized Ni_xCu_{1-x}Fe₂O₄.

2.2. Materials characterization

The X-ray diffraction patterns of the samples were identified using X-ray Diffractometer (XRD-6000 from Shimadzu, Japan) using Cu Kα radiation (λ = 1.5406 Å), with (2θ) = 10°- 80° in steps of 5 deg/s. Spectra of the powders were recorded using FTIR spectrometer (FTIR 8400S from Shimadzu, Japan) in the wave number range of 400-3500 cm⁻¹ to confirm the spinel structure of the samples. The surface morphology was analyzed through the use of FE-SEM (QUANTA 400, USA, 0.5- 30 kV) and TEM (CM120 Philips, Netherlands). The magnetic properties of CuNi ferrites were investigated using VSM (Cryogenic Limited PPMS, UK) under the applied field of ±1 (T). LCR meter (GW INSTRON LCR-8105G, Taiwan) was used to measure dielectric properties at a frequency range of 20Hz-3MHz.

3. Results and discussion

3.1. XRD and FTIR Analyses

Figure 1-(a, c, and d) shows XRD patterns of the Ni_xCu_{1-x}Fe₂O₄ nanoparticles (x= 0.0, 0.4, 1.0) calcinated at 200, 450, 650, and 850 °C for 3 h. The XRD patterns for all samples confirmed the appearance of major crystal planes of spinel ferrite at 850 °C. The experimentally calculated values of d-spacing and relative intensities of all reflection peaks were fully compatible with the standard JCPDS Card no (54-0964), (34-0425), and (25-1049) for nickel, copper, and Ni-Cu ferrites, respectively. For all the samples prepared and calcinated at different temperatures, it was noticed that when the temperature was increased, the peak of the reflections became sharper. This indicates an improvement in the crystallinity when the calcinating temperature increases. Additionally, it is noticed that as the calcinating temperature increases, the width of the central maxima decreases. This is due to the grain size increase with the increase in the calcinating temperature. The lattice constant (a) was calculated using equations (1) and (2) for cubic and tetragonal structures, respectively [13, 14]:

$$a = d\sqrt{h^2 + k^2 + l^2} \tag{1}$$

$$\frac{1}{d^2} = \frac{h^2 + k^2}{a^2} + \frac{l^2}{c^2} \tag{2}$$

where *d* is the interplanar spacing, *h*, *k*, and *l* are Miller indices, and *a* and *c* are lattice constants. The crystallite size (*D*) was calculated using the high intensity peak for all the compositions using Scherrer’s formula [15]:

$$D = \frac{K\lambda}{\beta \cos\theta} \tag{3}$$

where *k* is the shape factor (0.9), λ is the wavelength (1.5406 Å, CuKα), β is the full width at half maximum (FWHM), and θ is the diffraction angle.

X-ray density (ρ_{x-ray}) and surface area (*S*) of the ferrite samples were calculated by using the following formulas [16, 17]:

$$\rho_{x-ray} = \frac{8M}{N_A a^3} \tag{4}$$

$$S = \frac{6}{\rho_{x-ray} D} \tag{5}$$

where *M* is the molecular weight of the sample, *N* is the Avogadro’s number, and *a* is the lattice constant.

The values of the lattice constant, crystallite size, unit cell volume, X-ray density, and surface area of the calcinated samples are summarized in Table-1.

From Table-1, we can observe that x-ray density increases, while surface area decreases, with increasing calcinating temperature. Figure-1 (a) shows XRD patterns of pure NiFe₂O₄ nanoparticles that possess sharp characteristic diffraction peaks of (111), (220), (311), (222), (400), (422), (511), (440), and (533) reflection planes at 2θ values of 18.4°,30.3°,35.7°,37.3°,43.4°,53.9°,57.4°,63.1°, and

74.6°, respectively, which can be attributable to face-centered cubic phase (space group $Fd\bar{3}m$). An impurity phase of hematite ($\alpha\text{-Fe}_2\text{O}_3$) (JCPDS Card no 025-1402) is observed for the sample Ni-ferrite at 650 °C. The treatment by high-temperature at 850 °C caused the disappearance of the impurity phase and the formation of a single-phase of Ni-ferrite. Figure-1 (c) shows the XRD profile of the CuFe_2O_4 nanoparticles. The peaks that appear at 2θ range of 18.3°, 29.9°, 30.5°, 34.7°, 35.8°, 37.1°, 41.8°, 43.7°, 55.4°, 57.8°, 62.1°, 63.6°, and 74.6° correspond to the reflection planes (101), (112), (200), (103), (211), (202), (004), (220), (105), (321), (224), (400), and (413), respectively. The XRD shows that the crystal structure was deformed at 650°C from the cubic into a tetragonal system, with a secondary phase that belongs to CuO at 38.7 (JCPDS Card no 48-1548). Figure-1 (e) shows the XRD patterns of the $\text{Ni}_{0.4}\text{Cu}_{0.6}\text{Fe}_2\text{O}_4$ sample. It was observed that the sample possesses a face-centered cubic structure, with a space group symmetry of $Fm\bar{3}m$ (JCPDS Card no (25-1049)). The peaks appear at 2θ range of 18.3°, 30.1°, 35.5°, 37.1°, 43.2°, 53.6°, 57.1°, 62.7°, and 74.2° which correspond to the reflection planes (111), (220), (311), (222), (400), (422), (511), (440), and (533), respectively. It can be noted clearly that the crystalline volume increases with the increase in doping concentration of Cu, which may be due to a larger ionic radius of Cu^{2+} (0.73 Å) compared with that of Ni^{2+} (0.69 Å) [18-20]. On the other hand, the crystalline volume increases with increasing calcinating temperature, which is due to crystal growth. Values of the lattice parameter a for NiFe_2O_4 and $\text{Cu}_{0.6}\text{Ni}_{0.4}\text{Fe}_2\text{O}_4$ samples were found to be equal to 8.310 and 8.371 Å, respectively. The higher a value for $\text{Cu}_{0.6}\text{Ni}_{0.4}\text{Fe}_2\text{O}_4$ compared with that of NiFe_2O_4 is also due to the larger ionic radius of Cu^{2+} than that of Ni^{2+} . On the other hand, the lattice constant decreases with increasing calcinating temperature.

Table 1-Average crystalline size, lattice constant, unit cell volume, $\rho_{x\text{-ray}}$, space group, and surface area of $\text{Ni}_x\text{Cu}_{1-x}\text{Fe}_2\text{O}_4$ ($x = 0, 0.4, \text{ and } 1.0$) at different temperatures.

Samples	Temperature (°C)	Average crystalline size (nm)	Lattice constant (Å)	Unit cell volume (Å ³)	$\rho_{x\text{-ray}}$ (gm.cm ⁻³)	Space Group	Surface area (m ² .gm ⁻¹)
NiFe_2O_4	200	27.40	8.334	578.8	5.37	-	4.07
	450	34.50	8.357	583.6	5.33	-	3.26
	650	38.40	8.310	573.8	5.42	$Fd\bar{3}m$	2.88
	850	38.70	8.310	573.8	5.42	$Fd\bar{3}m$	2.86
$\text{Ni}_{0.4}\text{Cu}_{0.6}\text{Fe}_2\text{O}_4$	200	25.60	8.365	585.3	5.38	-	4.35
	450	29.10	8.364	585.1	5.38	-	3.83
	650	33.70	8.371	586.5	5.37	$Fm\bar{3}m$	3.31
	850	43.00	8.371	586.5	5.37	$Fm\bar{3}m$	2.59
CuFe_2O_4	200	17.90	8.359	584.0	5.44	-	6.16
	450	28.50	8.310	573.8	5.53	-	3.80
	650	34.00	5.830	294.3	10.76	141am d	1.64
	850	48.00	5.830	294.3	10.76	141am d	1.16

Figure-1 (b, d, and f) shows the FTIR spectra of $\text{Ni}_x\text{Cu}_{1-x}\text{Fe}_2\text{O}_4$ ($x = 0.0, 0.4 \text{ and } 1.0$) samples at calcinating temperatures of 200, 450, 650, and 850 °C for 3 h. The gels are mostly amorphous (noncrystalline) in nature but can be crystallized by heat treatment [21]. Therefore, when the temperature was raised to 200 °C, the phase beginnings of all samples were shown respectively. On the other hand, as the temperature was increased, we observed a decrease in the intensity of the bands, indicating the disappearance of water molecules and organic groups from the sample. In the case of samples calcinated at 850 °C, we noticed the appearance of two strong absorption bands. One bond was in the high-frequency range (ν_1) due to the frequencies of the Fe-O bonds of the tetrahedral (A site) between 557 and 586 cm^{-1} . The other bond was in the low-frequency range (ν_2), which is attributed to the frequencies of the M-O bonds of the octahedral (B-site) between 418 and 430 cm^{-1} [22-25].

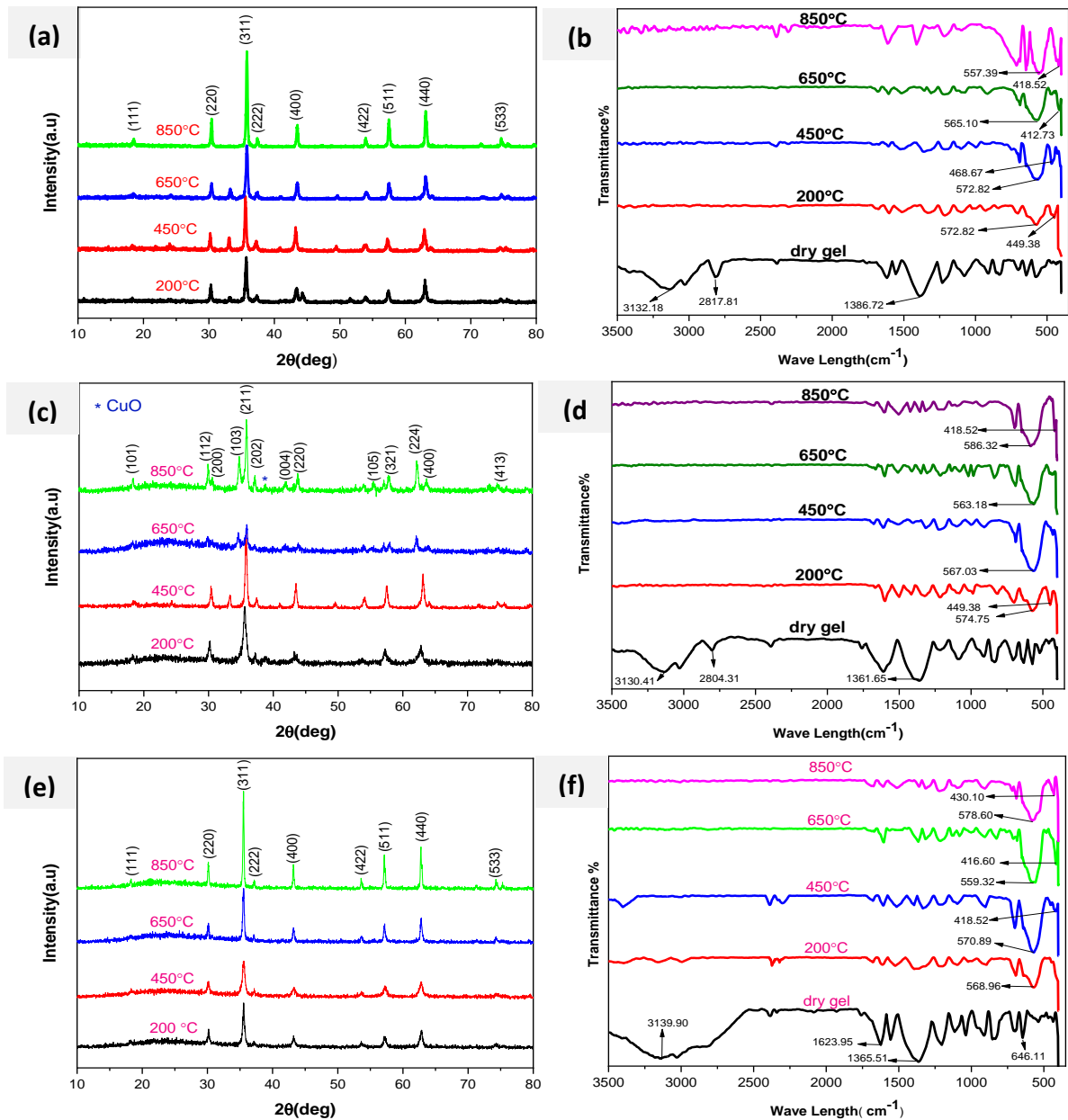


Figure 1 XRD patterns and FTIR spectra of (a)(b) NiFe₂O₄, (c)(d) CuFe₂O₄, and (e)(f) Ni_{0.4}Cu_{0.6}Fe₂O₄.

3.2. SEM and TEM Analysis

The morphology of the nanoparticles was examined through FE-SEM/EDX and TEM. Figure - shows SEM micrographs, the respective energy-dispersive X-ray spectroscopy (EDX), and the particle diameter distribution of NiFe₂O₄, CuFe₂O₄, and Ni_{0.4}Cu_{0.6}Fe₂O₄ nanoparticles calcinated at 850 °C. As can be seen from Figure-2 (a), pristine NiFe₂O₄ nanoparticles exhibit polyhedron and spheric morphology, some being accumulated to form larger particles. This agglomeration reduces the surface area of NiFe₂O₄ nanoparticles. Figure-2 (b) reveals the diameter histogram for NiFe₂O₄ nanoparticles, which displays a homogenous particle size distribution around 35.5nm range. Figure-2 (d) shows the SEM micrograph of CuFe₂O₄ nanoparticle, revealing a polyhedron shape with few agglomerations and negligible porosity. Figure-2 (e) shows a broad histogram of particle diameter distribution of CuFe₂O₄, with average size around 77.7nm. Figure-2 (g) displays the SEM image of Cu-substituted in Ni ferrites. The Ni_{0.4}Cu_{0.6}Fe₂O₄ sample shows uniform grain size distribution with average size around 40.6 nm (Figure-2(h)). Additionally, the image shows the presence of gaps caused by the release of

gases during the combustion process, such as CO₂, H₂O, etc. It should be noted now that the average diameter of the Ni_xCu_{1-x}Fe₂O₄ nanoparticles increases with increasing Cu²⁺ contents from 35.5 to 40.6 and 77.7 nm for x= 1.0, 0.4, and 0.0, respectively. The grain size of all samples was calculated by Image J software. The chemical composition of the synthesized samples was determined by EDX analysis. Figure- 2 (c) shows the EDX spectrum of NiFe₂O₄ compound, which indicated the presence of Ni, Fe, and O elements in the sample, where the atomic ratio of Ni and Fe was about 1:2. Figure-2 (f) shows the EDX spectrum of CuFe₂O₄ compound. We observe the presence of Cu, Fe, and O peaks, which are related to the CuFe₂O₄ nanoparticles. The Fe: Cu ratio was 2:1, which is consistent with theoretical calculations. On the other hand, the EDX spectrum analysis of Ni_{0.4}Cu_{0.6}Fe₂O₄ compound elements showed spectra for Cu, Ni, Fe, and O. All the samples displayed small amounts of the carbon component produced by the organic compound residue.

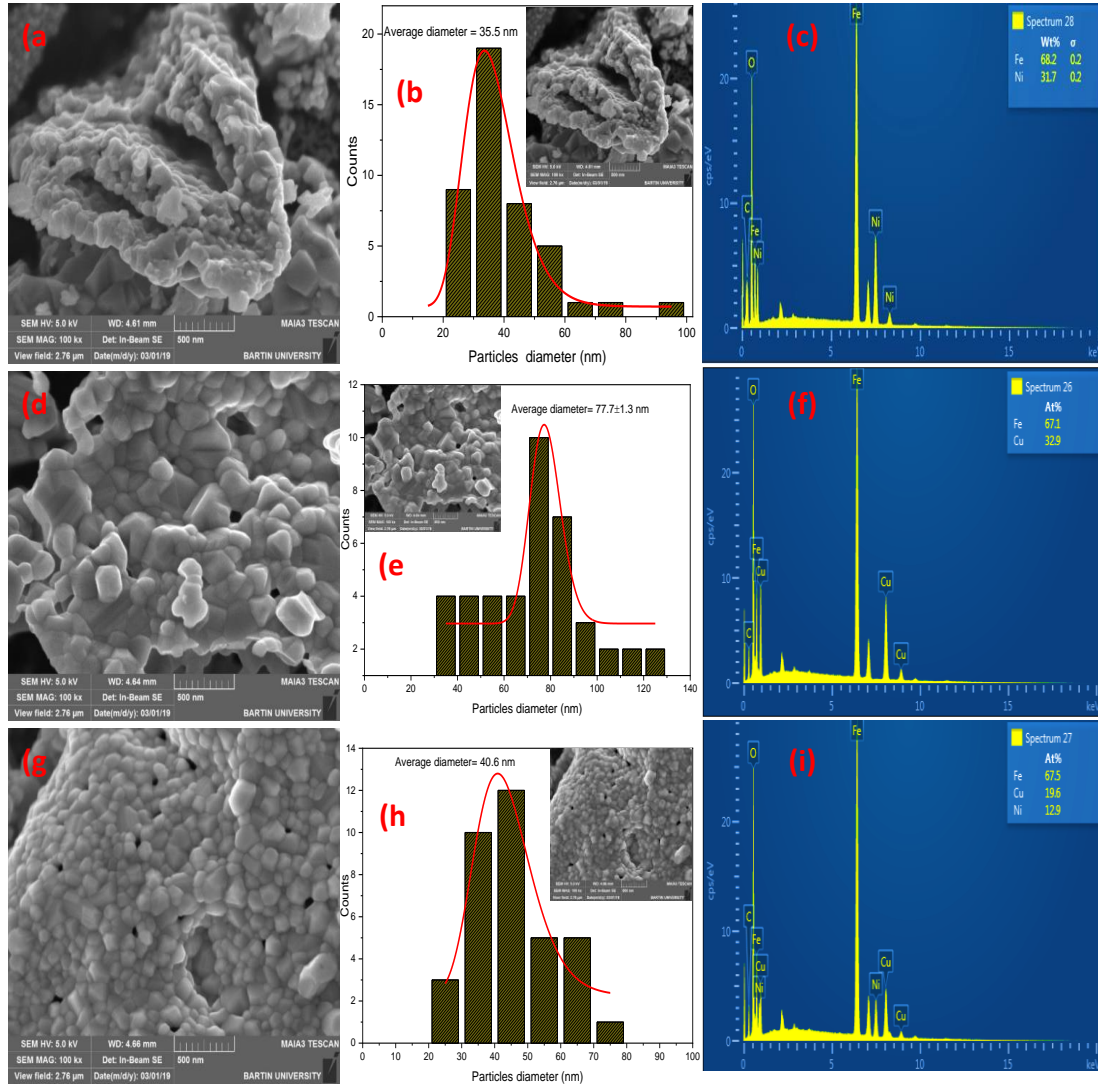


Figure 2-SEM-EDX micrographs and the particles diameter distribution of (a, b, c) pristine NiFe₂O₄, (d, e, f) pristine CuFe₂O₄, and (g, h, i) Ni_{0.4}Cu_{0.6}Fe₂O₄.

Figure-3 (a-f) shows TEM morphology images of NiFe₂O₄, CuFe₂O₄, and Ni_{0.4}Cu_{0.6}Fe₂O₄ nanoparticles calcinated at 850 °C. It is observed that most of the particles appear in spherical or polyhedron shapes. This depends on the ratio of Cu²⁺ cations substitution, where the compound NiFe₂O₄ gave more regular form while the compound Ni_{0.4}Cu_{0.6}Fe₂O₄ showed clear agglomerations. These agglomerations cause an increase in particle size.

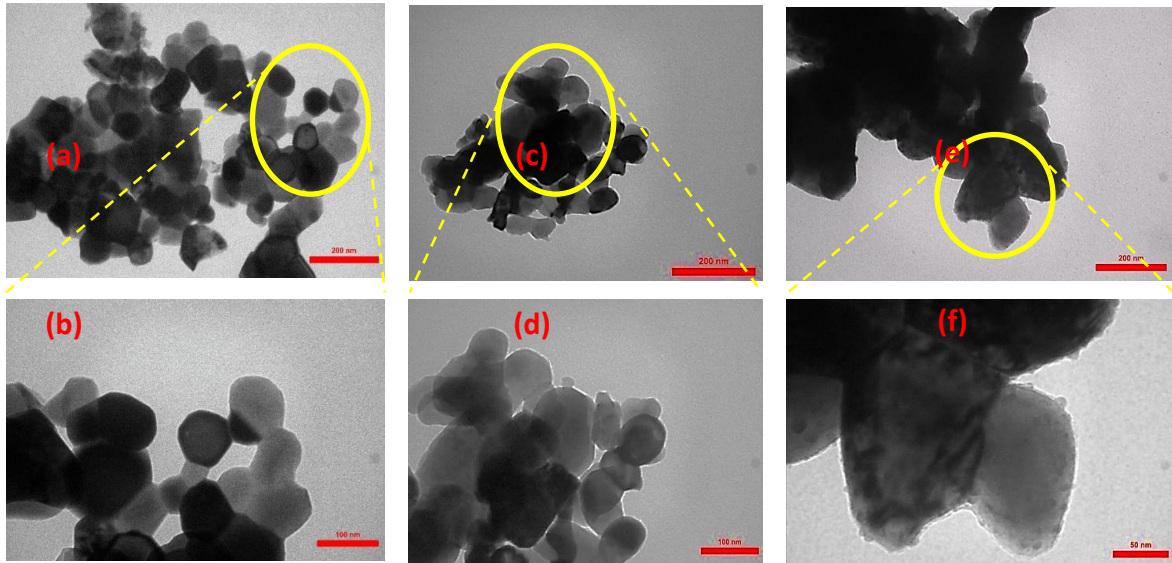


Figure 3 TEM micrographs at different magnifications of (a, b) pristine NiFe_2O_4 , (c, d) pristine CuFe_2O_4 , and (e, f) $\text{Ni}_{0.4}\text{Cu}_{0.6}\text{Fe}_2\text{O}_4$.

3.3. VSM Analysis

Figure-4 shows the magnetic hysteresis curve of $\text{Ni}_x\text{Cu}_{1-x}\text{Fe}_2\text{O}_4$ ($x = 0.0, 0.4, 1.0$) calcinated at 850°C . It is observed that all synthesized samples have the behavior of superparamagnetic status. The M_s value of the soft ferrite mainly depends upon the net magnetization of the spinel lattice. Magnetic properties of the Cu^{2+} ions-substituted nickel ferrite depend inherently on cation distribution in the lattice of the ferrites. The magnetic properties, such as M_s , H_c , and M_r were affected by Cu^{2+} ion concentration. Magnetic parameters extracted from VSM data at room temperature are summarized in Table-2. The M_s value of NiFe_2O_4 nanoparticles was 42.25 emu.g^{-1} , which was high as compared to the value in other samples. While the M_s value of CuFe_2O_4 nanoparticles was the lowest, being around 32 emu.g^{-1} . This might be due to the presence of CuO as an impurity, which was in fact detected in XRD analysis. Additionally, this could be due to the smaller magnetic moment of Cu^{2+} ion ($1.37\mu_B$). However, CuFe_2O_4 still has a high saturation magnetization. The experimental magnetic moment per formula unit (μ_B) in Bohr magneton was calculated using the following relation [26]:

$$\mu_B = \frac{MM_S}{5585} \quad (6)$$

As related to remnant magnetization, we noticed that the highest value was recorded for CuFe_2O_4 , followed by NiFe_2O_4 , and $\text{Cu}_{0.6}\text{Ni}_{0.4}\text{Fe}_2\text{O}_4$, respectively. Coercivity value was increased with the substitution of Cu^{2+} ions into Ni-ferrite and the highest value was recorded in CuFe_2O_4 due to the potential for a cationic disturbance on the surface [27]. In general, NiFe_2O_4 has an inverse spinel structure with Ni^{2+} ions in octahedral sites, and Fe^{3+} ions are equally distributed between tetrahedral and octahedral sites [28]. CuFe_2O_4 has a partial inverse spinel structure with 85% of Cu^{2+} are occupying octahedral sites, while the other 15% are occupying tetrahedral sites. However, Fe^{3+} ions are equally distributed in the tetrahedral and octahedral sites [29]. This means that the Ni^{2+} ions have a strong preference for octahedral sites, while Cu^{2+} ions have a similar preference for octahedral and tetrahedral sites. When Cu^{2+} is substituted by Ni^{2+} in $\text{Ni}_x\text{Cu}_{1-x}\text{Fe}_2\text{O}_4$ nanoparticles, the cation distribution will change and thus changes the magnetic properties subsequently. Table-2 shows that ferrite samples have various coercivity values. This may be attributed to several reasons, such as composition, surface conditions, and magnetic anisotropy.

The squareness ratio ($Sq = M_r/M_s$) was increased with increasing the content of Cu. Therefore, the maximum Sq value was found to be 0.46, indicating the enhanced contribution from the cubic anisotropy for CuFe_2O_4 . Hence, a large coercivity can be expected for CuFe_2O_4 . The values of anisotropy constant (K) were evaluated using the following relation [30, 31]:

$$H_c = \frac{0.96 K}{M_s} \tag{7}$$

The anisotropy constant was observed to increase with increasing Cu²⁺ content.

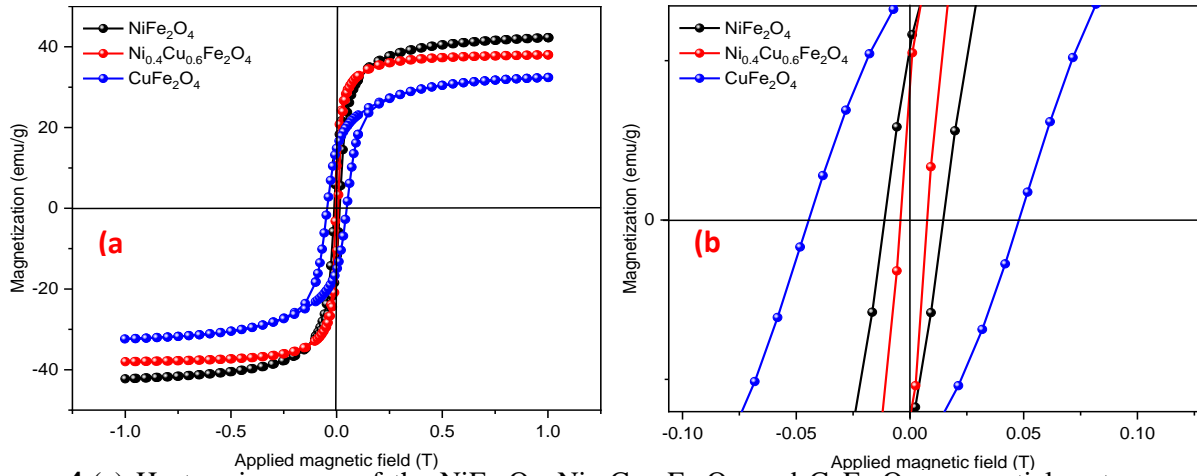


Figure 4-(a) Hysteresis curves of the NiFe₂O₄, Ni_{0.4}Cu_{0.6}Fe₂O₄, and CuFe₂O₄ nanoparticles at room temperature. (b) enlarged view of the M–H curve that shows the coercive fields.

Table 2-Saturation magnetization (*M_s*), remanence (*M_r*), coercivity (*H_c*), squareness (*S_q*), magnetic moment (*μ_B*), and anisotropy constant (*K*) of Ni_{*x*}Cu_{1-*x*}Fe₂O₄ ferrites (*x* = 0,0.4,1.0) calcinated at 850 °C for 3 h.

Sample	<i>M_s</i> [emu.g ⁻¹]	<i>M_r</i> [emu.g ⁻¹]	<i>H_c</i> [O _e]	<i>S_q</i>	<i>μ_B</i>	<i>K</i> × 10 ⁻³ [emu.O _e g ⁻¹]
NiFe ₂ O ₄	42.25	11.64	165.91	0.27	1.76	7.302
Ni _{0.4} Cu _{0.6} Fe ₂ O ₄	37.99	10.49	57.33	0.27	1.61	2.269
CuFe ₂ O ₄	32.00	14.87	517.16	0.46	1.37	17.449

3.4. Dielectric Properties

AC electrical properties, represented by the real part of dielectric constant (*ε'*), the imaginary part of dielectric constant (*ε''*) and the loss factor (*tanδ*), in addition to the alternating conductivity (*σ_{ac}*) of the samples of NiFe₂O₄, Ni_{0.4}Cu_{0.6}Fe₂O₄, and CuFe₂O₄, were studied as a function of frequency at room temperature in a frequency range of 20Hz-3MHz. The real and imaginary dielectric constant values were calculated by using the following equations [32]

$$\epsilon' = \frac{C d}{\epsilon_0 A} \tag{8}$$

$$\epsilon'' = \epsilon' \tan \delta \tag{9}$$

where *C* is the capacitance of the pellet, *d* is the thickness, *A* is the cross-sectional area, and *ε₀* is the permittivity of free space (*ε₀* = 8.854 × 10⁻¹² F.m⁻¹). Figure-5 (a and b) shows the variation of dielectric constant and imaginary part with frequency. It is seen that the real and imaginary dielectric constant values of the samples decrease with increasing frequency and then they remain constant at high values, which is the normal behavior of most ferrites. The high values of the real dielectric constant at low frequencies are due to the polarization of the space charge due to the large mass of its dipoles compared to other types of polarization (electronic, ionic, and directional). When the frequency is increased, these dipoles cannot rotate with the electric field and thus the dielectric constant decreases. This behavior of ferrite has been observed by many researchers [33-35]. Figure- 4 also shows that the highest value of the real dielectric constant was recorded for CuFe₂O₄ (24304) and the lowest value was for NiFe₂O₄ (2323), whereas that for Ni_{0.4}Cu_{0.6}Fe₂O₄ mediated the two values. Since ferrite has a semi-conductive nature, this is affected by doping with other atoms. The effect of doping on charge carriers is either reflected by an increase or a decrease in the real dielectric constant, depending on the type of atom. Therefore, the dielectric constant values differed as a result of the nickel doping process.

The loss factor is a measure of energy dissipation within the dielectric medium and is considered as

part of the primary loss in the ferrite. We notice from Figure-5 (c) that the maximum values of the loss factor and the loss tangent appeared at low frequencies, while they were decreased with the increase in frequency, until they became constant and stable. Similar results were observed in another research of ferrite systems [36]. This result of the distribution of values in the curve of the imaginary dielectric constant and loss factor is attributed to the Maxwell-Wagner theory of interpolarity [37]. According to this theory, the dielectric constant of ferritic materials consists of two layers, namely the grains and grain boundaries, where the grains are considered regions with low electrical resistance, due to the ideal crystalline properties, while grain boundaries are regions with high resistance. According to Maxwell-Wagner polarization theory, the polarization between surfaces within the grain boundaries occurs due to the accumulation of charge in these high-resistance boundaries. This polarization occurs in all heterogeneous crystalline materials (which are more than one phase). Figure-5 (d) shows the alternating electrical conductivity, as this study provides important information about this process and the effect of deformation on it. In general, the conduction process occurs in the ferrite materials as a result of the transfer of electrons between Fe^{+2} and Fe^{+3} located in octagonal locations [38]. The values of AC conductivity (σ_{ac}) were calculated using the following equation [32, 39]:

$$(\sigma_{ac}) = \omega \epsilon_0 \epsilon' \tan \delta \tag{10}$$

where ω is the angular frequency. Figure-5 (d) shows that AC conductivity decreases with the addition of nickel atoms, as electronic transitions between Fe^{+2} and Fe^{+3} decrease in the octagonal locations [39]. On the other hand, grain boundaries in the low conduction operate in all samples at frequencies of 10^3 - 10^4 Hz where the transmission of electrons between Fe^{+2} and Fe^{+3} decreases relatively, while electronic mobility increases in the larger frequencies (10^4 Hz) as the grain boundaries become more active, which enhances conductivity.

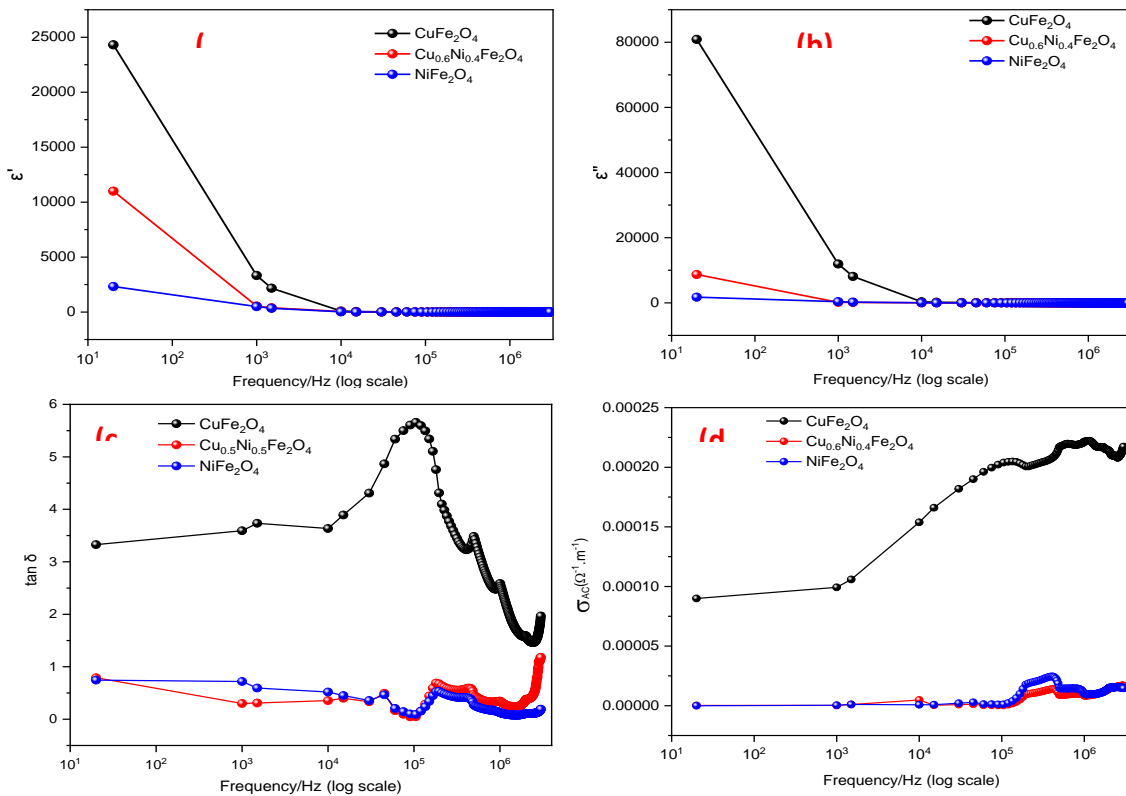


Figure 5 Frequency dependent (a) real part of dielectric constant, (b) imaginary part of dielectric constant, (c) loss factor, and (d) AC conductivity of $Ni_xCu_{1-x}Fe_2O_4$ ($x = 0, 0.4, 1.0$).

4. Conclusions

The $Ni_xCu_{1-x}Fe_2O_4$ ($x = 0.0, 0.4, \text{ and } 1.0$) nanoparticles were synthesized successfully via the citrate-gel auto combustion method. These Ni-Cu ferrite nanoparticles show polyhedron and spherical morphology as revealed via SEM and TEM results. XRD analysis exhibited deformation in system structure, from cubic to tetragonal system, when substituting Cu^{2+} cations in nickel ferrite completely at $850^\circ C$. The Cu content has a significant effect on dielectric and magnetic properties, where the

substitution of copper in nickel ferrite decreases the saturation magnetization and improves dielectric properties of nickel ferrite. Thus, we obtained superb ferrite materials that have mixed properties from Ni-ferrite and Cu-ferrite, which make them good materials for electronic applications, including sensors, EM devices operating at high frequencies, and magnetic fluids.

References

1. Ramankutty, C.G. and Sugunan, S. A. **2001**. Surface properties and catalytic activity of ferros spinels of nickel, cobalt and copper, prepared by soft chemical methods, *Applied Catalysis A: General*, **218**(1-2): 39-51.
2. Zuo, X., Yang, A., Vittoria, C. and Harris, V.G. **2006**. computation study of copper ferrite, *Journal of applied physics*, **99**, 0.8M909.
3. Sun, Z., Liu, L., Jia, D. Z. and Pan, W. **2007**. simple synthesis of CuFe_2O_4 nanoparticles as gas-sensing materials, *Sensors and Actuators B Chemical*, **125**(1): 144-148.
4. Sun, S., Zeng, H., Robinson, D.B., Raoux, S., Rice, P.M., Wang, S.X. and Li, G. **2004**. Mono-disperse MFe_2O_4 (M=Fe, Co, Mn) nanoparticles, *Journal of the American Chemical Society*, **126**: 273-279
5. Standley, K.J. **1972**. *Oxide Magnetic Materials*. second Edition. Clarendon Press Oxford.
6. Mazen, S.A. **2000**. Tetravalent ions substitution in Cu – ferrite; structure formation and electrical properties, *Materials Chemistry and Physics*, **62**(2): 131-138.
7. Erb, U. **1995**. Electrodeposited nanocrystals: Synthesis, properties and industrial applications, *Nanostructured Materials*, **6**: 533-538.
8. Komarneni, S., D'Arrigo, M.C. Leionelli, C., Pellacani, G.C. and Katsuki, H. **1998**. Microwave-Hydrothermal Synthesis of Nanophase Ferrites. *Journal of the American Ceramic Society*, **81**(11): 3041-3043.
9. Sartale, S.D. and Lokhande C.D. **2000**. Room temperature preparation of NiFe_2O_4 thin films by electrochemical route, *Indian Journal of Engineering and Materials Sciences*, **7**(5): 404-410.
10. Hu, J., Yan, M. and Zhang, W. **2006**. Effect of calcination on the magnetic permeability of $(\text{Ni}_{0.21}\text{Zn}_{0.58}\text{Cu}_{0.23})\text{Fe}_{1.95}\text{O}_4$ ferrite prepared using the sol-gel self-propagated technique, *Materials Chemistry and Physics*, **98**(2-3): 459-462.
11. Sartale, S.D. and Lokhande, C.D. **2001**. Electrochemical deposition and oxidation of CuFe_2 alloy: a new method to deposit CuFe_2O_4 thin films at room temperature. *Materials Chemistry and Physics*, **70**(3): 274-284.
12. Roy, P.K. and Bera, J. **2007**. Enhancement of the magnetic properties of Ni – Cu-Zn ferrites with the substitution of a small fraction of lanthanum for iron, *Materials research bulletin*, **42**(1): 77-83.
13. Bayrakdar, H., Yalçın, O., Vural, S. and Esmer, K. **2015**. Effect of Cu doped nickel ferrites on structural, magnetic and dielectric properties, *Materials Today: Proceedings*, **2**: 5559 – 5567
14. Kanagaraj M., Sathishkumar P., Selvan G.K., Kokila I.P. and Arumugam S. **2014**. Structural and magnetic properties of CuFe_2O_4 as-prepared and thermally treated spinel nanoferrites, *Indian Journal of Pure & Applied Physics*, **52**: 124-130.
15. Rao, P., Godbole, R.V. and Bhagwat, S. **2016**. Copper doped nickel ferrite nano-crystalline thin films: A potential gas sensor towards reducing gases, *Materials Chemistry and Physics*, **171**: 260-266
16. Naidu, K.Ch. B. and Madhuri, W. **2017**. Hydrothermal synthesis of NiFe_2O_4 nano-particles: structural, morphological, optical, electrical and magnetic properties, *Bulletin of Materials Science*, **40**: 417-425.
17. Otterstedt, J.-E., Brandreth, D.A. **1998**. *Small Particles Technology*. New York. Plenum Press.
18. Ata-Allah, S.S. and Kaiser, M. **2009**. Conductivity and dielectric studies of copper-aluminate substituted spinel nickel ferrite, *Journal of Alloys and Compounds*, **471**(1-2): 303-309.
19. Mazen, S., Abd Allah, M., Nakhla, R.I., Zaki, H.M. and Matawe F. **1993**. X-ray analysis and IR absorption spectra of Li-Ge ferrite, *Materials Chemistry and Physics*, **34**(1): 35-40.
20. Amer, M.A., Meaz, T.M., Attalah, S.S. and Ghoneim, A.I. **2014**. Structural and magnetic characterization of the $\text{Mg}_{0.2-x}\text{Sr}_x\text{Mn}_{0.8}\text{Fe}_2\text{O}_4$ nanoparticles, *Journal of magnetism and magnetic materials*, **363**: 60-65.

21. Shirsath, S. E., Jadhav, S. S., Mane, M. L., and Li, S. **2016**. *Ferrites Obtained by Sol–Gel Method. Handbook of Sol-Gel Science and Technology*. Cham. Springer.
22. Waldron, R.D. **1955**. Infrared spectra of ferrites, *Physical Review Journals Archive*, **99**: 1727-1735.
23. Thummer, K.P., Pandya, M.P., Jani, K.H., Modi, K.B. and Joshi, H.H. **2004**. Microscope and Macroscopic Magnetic Properties of the $MgAl_xCr_xFe_{2-2x}O_4$ Spinel Ferrite System, *Materials Science*, **40**(1): 102-112.
24. Guo, L., Shen, X., Meng, X., Feng, Y. **2010**. Effect of Sm^{3+} ions doping on structure and magnetic properties of nanocrystalline $NiFe_2O_4$ fibers, *Journal of Alloys and Compounds*, **490**(1): 301-306.
25. Nakamoto, K. **2006**. *Infrared and Raman spectra of inorganic and coordination compounds. Handbook of Vibrational Spectroscopy*. John Wiley & Sons, Ltd.
26. Manju B.G. and Raj, P. **2019**. Green Synthesis of Nickel–Copper Mixed Ferrite Nanoparticles: Structural, Optical, Magnetic, Electrochemical and Antibacterial Studies, *Journal of Electronic Materials*, **48**(12): 7710-7720
27. Rais, A., Taibi, K., Addou, A., Zanon, A. and Al-Douri, Y. **2014**. Copper Substitution Effect on the Structural Properties of Nickel Ferrites, *Ceramics International*, **40**: 14413-14419.
28. Perron, H., Mellier, T., Domain, C., Roques, J., Simoni, E., Drot, R. and Catalette, H. **2007**. Structural investigation and electronic properties of the nickel ferrite $NiFe_2O_4$: A periodic density functional theory approach, *J. Phys.: Condens. Matter*, **19**: 1-10.
29. Zuo, X., Yang, A., Vittoria, C., and Harris, V. G. **2006**. Computational study of copper ferrite ($CuFe_2O_4$), *J. Appl. Phys.*, **99**(8): 1-3.
30. Yadav R. S., Kuřitka, I., Jarmila, V., Havlica, J., Masilko, J., Kalina, L., Tkacz, J., Švec, J., Enev V. and Hajdúchová, M. **2017**. impact of grain size and structural changes on magnetic, dielectric, electrical, impedance and modulus spectroscopic characteristics of $CoFe_2O_4$ nanoparticles synthesized by honey mediated sol-gel combustion method, *Advances in Natural Sciences: Nanoscience and Nanotechnology*, **8**(4): 1-14.
31. Stoner, E.C. and Wohlfarth, E.P. **1948**. A mechanism of magnetic hysteresis in heterogeneous alloys, *Philos Trans R Soc London Ser A* **240**: 599. Reprinted by *IEEE Trans Magn* **27**: 3475 (1991).
32. Anjum, S., Rashid, A., Bashir, F., Pervaiz, M. and Zia, R. **2015**. Effect of Cu Doped Nickel Ferrites on Structural, Magnetic and Dielectric Properties, *Materials Today: Proceedings*, **2**(10): 5559-5567.
33. Kumar, A. and Yadav, K.L. **2011**. Magnetic, magnetocapacitance and dielectric properties of Cr doped bismuth ferrite nanoceramics, *Materials Science and Engineering*, **176**(3): 227-230.
34. Malik, H., Khan, M. A., Hussain, A., Warsi, M. F., Mahmood, A., and Ramay, S. M. **2018**. Structural, spectral, thermal and dielectric properties of Nd-Ni co-doped Sr-Ba-Cu hexagonal ferrites synthesized via sol-gel auto-combustion route. *Ceramics International*, **44**(1): 605-612.
35. Omri, A., Dhahri, E., Costa, B.F.O., and Valente, M.A. **2020**. Structural, Electric and Dielectric properties of $Ni_{0.5}Zn_{0.5}FeCoO_4$ ferrite prepared by sol-gel, *Journal of Magnetism and Magnetic Materials*, **499**: 1-28.
36. Wang, Y., Zhu, J., Zhang, L., Yang, X. and Wang, X. **2006**. Preparation and characterization of perovskite $LaFeO_3$ nanocrystals, *Materials Letters*, **60**(13-14): 1767-1770.
37. Thomas, N., Jithin, P. V., Sudheesh, V. D. and Sebastian, V. **2017**. Magnetic and dielectric properties of magnesium substituted cobalt ferrite samples synthesized via one step calcination free solution combustion method, *Ceramics International*, **43**(9): 7305-7310.
38. Farea, A.M.M., Khalid, Sh.K., Bato, M., Yousef, A., GyuLee, Ch. and Alimuddin, R. **2009**. Influence of the doping of Ti^{4+} ions on electrical and magnetic properties of $Mn_{1+x}Fe_{2-2x}Ti_xO_4$ ferrite, *Journal of Alloys and Compounds*, **469**(1-2): 451-457.
39. Dahham, N. A., Abdul-Aziz, Ab. F. and Jasim A. S. K. **2017**. Fabrication And Studies Of structural, Dielectrical Properties Of $(Ni_{0.95-x}Co_xCu_{0.05}Fe_2O_4)$ Composites by Powder Technology Method, *Tikrit Journal of Pure Science*, **22**(11): 48-54.